Journal of
Synchrotron
Radiation

ISSN 1600-5775

Received 28 February 2014
Accepted 29 April 2014

A multiplexed high-resolution imaging spectrometer for resonant inelastic soft X-ray scattering spectroscopy

Tony Warwick,* Yi-De Chuang, Dmitriy L. Voronov and Howard A. Padmore

Advanced Light Source, Lawrence Berkeley National Laboratory, Berkeley, CA 94720, USA.
*E-mail: warwick@lbl.gov

The optical design of a two-dimensional imaging soft X-ray spectrometer is described. A monochromator will produce a dispersed spectrum in a narrow vertical illuminated stripe (~2 μm wide by ~2 mm tall) on a sample. The spectrometer will use inelastically scattered X-rays to image the extended field on the sample in the incident photon energy direction (vertical), resolving the incident photon energy. At the same time it will image and disperse the scattered photons in the orthogonal (horizontal) direction, resolving the scattered photon energy. The principal challenge is to design a system that images from the flat-field illumination of the sample to the flat field of the detector and to achieve sufficiently high spectral resolution. This spectrometer provides a completely parallel resonant inelastic X-ray scattering measurement at high spectral resolution (~30000) over the energy bandwidth (~5 eV) of a soft X-ray absorption resonance.

Keywords: soft X-ray; scattering; spectrometer.

1. Introduction

Resonant inelastic X-ray scattering (RIXS) spectroscopy, a photon-in/photon-out spectroscopy, is a powerful technique for studying elementary excitations in strongly correlated materials [see, for example, the review articles by Ament *et al.* (2011) and Kotani & Shin (2001)]. In the RIXS process, an incident photon with energy tuned close to an elemental absorption edge is used to excite a core electron into an unoccupied state. The resulting core hole breaks the local symmetry and strongly influences the nearby electronic structure. The core hole is quickly filled in by a valence electron, leaving the valence electronic structure disturbed from the ground state. This transient symmetry breaking has a strong interplay with surrounding many-body correlations, and extensive information about such correlations and dynamics can be obtained by analysing the energy, momentum and polarization state of the scattered photon (relative to the incident photon). Furthermore, resonance effects often greatly enhance electronic contributions in the RIXS signal, providing unique sensitivity to the elemental, chemical and orbital states of materials under study. Despite being such a powerful technique, progress in the application of RIXS spectroscopy has been limited by energy resolution and throughput.

Development of high-brightness third-generation synchrotron sources has led to advances in soft X-ray RIXS instrumentation. Low-emittance sources allow the use of highly demagnifying mirrors to produce micrometer-sized beams on the sample. With a small beam spot, the soft X-ray spectrometer can be operated in a slitless mode for high throughput (larger angular acceptance) with good energy resolution. To date, a reasonably sized spectrometer (a few meters in length) with $R > 10000$ can be constructed and such instruments have already revolutionized RIXS research (see, for example, publications at the ADRESS beamline website: http://www.psi.ch/sls/adress/publications). Various facilities (*e.g.* NSLS-II, Diamond, MAX IV) are now constructing new soft X-ray RIXS beamlines and spectrometers with unprecedented energy and momentum resolution, and enhanced throughput, to further expand this research frontier.

Even with these advances in instrumentation, RIXS spectra will be recorded in a sequential manner. The incident photon energy will be tuned prior to recording each RIXS spectrum, and the RIXS map, a two-dimensional intensity map showing RIXS features with respect to incident ($h\nu_{\rm in}$) and scattered ($h\nu_{\rm out}$) photon energies, is generated after running a sequence of $h\nu_{\rm in}$. In this mode of acquisition, the beamline exit slit is closed down to provide monochromatic light. One expects to have fewer data points along the $h\nu_{\rm in}$ axis (numbers of incident photon energies) than the $h\nu_{\rm out}$ axis (numbers of pixels on the spectrometer detector). The coarse sampling in $h\nu_{\rm in}$ might not seem to lead to a significant loss in information, yet the lessons learned from analysing angle-resolved photoemission spectroscopy (ARPES) data along the Momentum Distribution Curve (MDC) *versus* the Energy Distribution Curve (EDC)

suggest otherwise [for a review, see Damascelli *et al.* (2003)]. It has been shown that the elementary excitations can have strong $h\nu_{\rm in}$ dependence, and studying such dependence not only offers a metric to fingerprint the symmetries of excitations but can also reveal the underlying temporal dynamics that creates them (Chen *et al.*, 2010; Wray *et al.*, 2012).

If $h\nu_{\rm in}$ can be sampled at finely spaced intervals, in parallel, over the bandwidth of a RIXS resonance, and if this can be done simultaneously with fine parallel sampling in $h\nu_{\rm out}$, then a complete RIXS map can be measured in a single acquisition at high resolution and with a very large increase in throughput. This is a very attractive possibility for these low rate measurements. Recently, there have been designs developed for soft X-ray RIXS experiments to advance the technique in this direction. For example, the active-grating-monochromator/active-grating-spectrometer design (Fung *et al.*, 2004) at NSRRC, Taiwan, arranges the dispersion planes of both the beamline monochromator and the X-ray spectrometer to be vertical. The beamline and the spectrometer use identical dispersive optics in opposite order such that the dispersed light from the beamline at the sample surface can be recombined by the spectrometer at the detector, giving a high-throughput high-resolution measurement of the energy-loss spectrum. However, simultaneous measurement of both $h\nu_{\rm in}$ and $h\nu_{\rm out}$ is not possible.

Strocov (2010) proposed an optical scheme (termed $h\nu^2$) which arranges these two dispersion planes orthogonally. With this scheme, Strocov suggested that the RIXS map can be obtained in a parallel detection scheme with large throughput by imaging over a finite field on the sample, illuminated with dispersed light. The proposed scheme suffers from the fact that the focal length of grazing-incidence X-ray optics varies significantly across a finite object field. It is well known that a single grazing-incidence mirror will produce a focal plane that is tilted at close to the angle of incidence of the mirror and thus, for an imaging plane perpendicular to the principal ray, only the rays very close to the object axis will be sufficiently well focused. This defeats the two-dimensional imaging required in the spectrometer.

This problem of the obliquity of the image field was first recognized by Ernst Abbe (Abbe, 1879) who described a general condition (the Abbe sine condition) that has to be met by a flat-field imaging system. It states that if φ and φ' are the angles of the incoming and outgoing rays with respect to the symmetry axis and if the subscript p refers to the paraxial ray and if

$$\frac{\sin\varphi}{\sin\varphi'} = \frac{\varphi_{\rm p}}{\varphi'_{\rm p}}, \qquad (1)$$

then an optical system will be 'aplanatic' and can image an erect object onto an erect image field.

Hans Wolter (Wolter, 1952*a*,*b*) discovered several grazing-incidence focusing arrangements using two aspheric mirrors that approximately satisfy equation (1). He showed that for a source at infinity, a combination of a parabola and a hyperbola could be used to make an aplanatic system. His landmark result has been the basis for almost every X-ray telescope

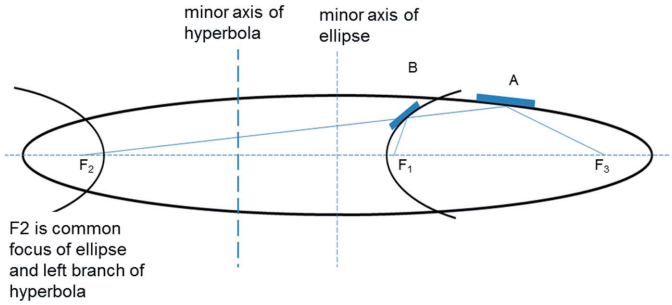

Figure 1
Wolter type 1 system for imaging a source at finite distance. Rays from F_1 are focused by a hyperbola making a virtual source at F_2 for imaging by an ellipse to the real image F_3. The magnification is (A–F3/A–F2) × (B–F2/B–F1).

(Saha, 1987), including the presently operating Chandra X-ray Observatory (see http://chandra.harvard.edu/). The arrangement has two basic configurations, one in which light collected on the inside of a parabolic surface is reflected from the concave inside of a hyperbolic surface (type 1) and one in which it is reflected from the convex outside of a hyperbolic surface (type 2). Most X-ray telescopes have used Wolter type 1 optics for ease of construction. For imaging a source at finite distance, as required here, the parabola is replaced by an ellipse. This optical scheme is illustrated in Fig. 1. Such modified Wolter systems have been developed for use with soft X-rays, to image laser-induced plasmas (Kodama *et al.*, 1996) and in pursuit of full-field X-ray imaging with a synchrotron source (Matsuyama *et al.*, 2010); but to our knowledge, they have not been used in conjunction with dispersive optics in a spectrometer, as proposed here.

In this paper we will take up Strocov's $h\nu^2$ idea and develop an advanced flat-field imaging design using aspheric mirrors in a Wolter geometry. These mirrors will image a vertical strip of the sample illuminated with incident photon energies dispersed across its surface in the vertical direction. The mirrors will be coupled with a high-resolution grating scheme to disperse and image the scattered photons in the orthogonal plane. A two-dimensional detector then displays the RIXS map with vertical and horizontal axes mapping the incident ($h\nu_{\rm in}$) and scattered ($h\nu_{\rm out}$) photon energies, respectively. Fig. 2 shows the scheme. The spectrometer is designed to provide a resolving power $R \simeq 30000$ with a total instrument length $\simeq$5 m. The angular acceptance is 5 mrad (vertical) by 9 mrad (horizontal).

2. Imaging requirements

The object plane for the spectrometer is the sample. Incident photons of different energy are focused vertically by a vertically dispersing beamline monochromator to different vertical positions on the sample, with the monochromatic source image being $\sim$5 µm high. This spatial structure must be relayed onto the spectrometer detector image plane without blurring. This is accomplished by a pair of aspheric Wolter

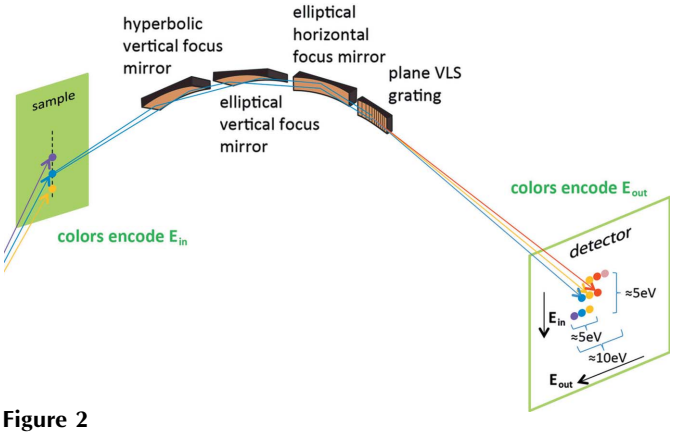

Figure 2
The spectrometer scheme. The color of the spots on the sample and on the detector ranges from violet through red and indicates increasing wavelength of the incident and scattered X-rays.

mirrors deflecting and focusing vertically, as described in more detail below.

At the same time, the beamline will focus the incoming X-rays in the orthogonal (horizontal) direction to a spot on the sample ~2 μm wide. This spot is the source for the dispersive optics in the spectrometer which must disperse and image to the same spectrometer detector image plane. This is accomplished by a focusing mirror and a varied line space (VLS) grating. There can be no wavelength dependence to this focal length if the orthogonal Wolter mirrors are to focus correctly across the operational wavelength range. This means that the image plane (the detector) must be orthogonal to the spectrometer optical axis (*i.e.* it must be erect).

A similar argument applies in the beamline, which disperses and focuses light to a (vertical) strip on the sample that must be orthogonal to the (horizontal) beamline optical axis. Both the spectrometer object plane (containing the illuminated strip of the sample) and the spectrometer image plane (the imaging detector chip) must be erect.

A key enabling technology for the system is the use of small-pixel X-ray detectors. Although CCD detector pixel size is limited to a minimum value around 10 μm by intrinsic restrictions in the charge transfer process, commercial CMOS detectors have been recently made with pixel sizes approaching 1 μm. The detector for this spectrometer will be based on a sensor that was developed for the TEAM aberration-corrected electron microscope at LBNL (Battaglia *et al.*, 2010; Contarato *et al.*, 2011) using a 0.18 μm CMOS process. This 760 × 768 pixel sensor has a pixel size of 5 μm, and is designed to be radiation hard. A version of this sensor has been back-thinned to the 10 μm thick epi-layer and will have an ultra-thin MBE front surface contact to ensure the highest soft X-ray transmission. A thicker-contact version of this new detector is presently undergoing tests with soft X-rays.

The small spots corresponding to the spectral resolution elements on the sample must be magnified by the Wolter mirrors (vertically, $M \simeq 5$) and by the dispersing optics (horizontally, $M \simeq 10$) to cover about five 5 μm detector pixels at normal incidence. This means that we oversample at ~2.5 times the Nyquist limit. These values of magnification can be achieved with a sufficiently large aberration-free field of view on the sample (vertically) and the required spectral resolution in the dispersive direction (horizontally).

3. The synchrotron beamline

A synchrotron beamline has been designed to illuminate this spectrometer. The choice of monochromator is important because an erect focal plane is required along with a very small horizontal spot size. The monochromator scheme adopted here uses a fixed focusing mirror and a VLS plane grating (Hettrick *et al.*, 1988; Amemiya *et al.*, 1996) in the vertical (dispersive) plane. The focal plane is approximately flat in this direction and can be arranged to be erect at the sample at a single design wavelength. A separate grating is provided for each edge/species allowing the grating efficiency to be specifically optimized, the focal plane to be precisely erect and to require only a small angular scan range. The optical scheme is almost the same as that of the spectrometer described below. In the horizontal direction a strongly de-focusing elliptical cylinder will produce a demagnified image of the undulator source two-thirds of the way down the beamline, where it can be defined with slits if necessary. This secondary source is further demagnified by a second elliptical cylinder outside the monochromator to form a 2.3 μm FWHM spot on the sample. The net horizontal demagnification is a factor of 175. The synchrotron source is sufficiently small in the horizontal direction that the aplanatism of these mirrors is not an issue.

Such a large demagnification produces a highly convergent beam. For example, at 260 eV the FWHM undulator divergence is 81 μrad. With 175:1 demagnification the FWHM convergence at the sample is 14 mrad. The grazing angle on the mirrors is 2° (35 mrad) so the convergent beam occupies less than half of the grazing angle. This is a criterion we have used in the design of other strongly focusing systems, and ensures that the reflectivity does not change significantly across the mirror. A second consequence is that the depth of field of the image is small, approximately ±80 μm. Centering of the sample in the steeply inclined focal plane of these horizontally focusing mirrors is important.

In the dispersive direction (vertical) this beamline provides a spectral-resolution element at $R \simeq 30000$ of 5.6 μm FWHM, focused at the sample with a dispersion across the sample surface of 4.5 eV mm^{-1} at 700 eV. A typical RIXS resonance in the soft X-ray regime between 250 eV and 1000 eV might be 5 eV wide and that bandwidth would illuminate the sample over a (vertical) strip about 1 mm high.

4. Imaging spectrometer optics

The total length of the spectrometer is designed to be 5 m and the layout is shown in Fig. 3. A modified Wolter type 1 scheme using an ellipse and a hyperbola will image in the non-dispersive (vertical) plane of the spectrometer. For the spectrometer, these mirrors must provide magnification ($M \simeq 5$) to map the 5 μm beamline resolution element onto several

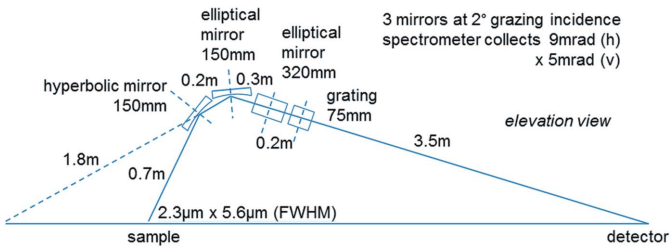

Figure 3
Spectrometer layout.

detector pixels. We use $M \simeq 5$ with a 5 μm detector pixel-size to over-sample the Nyquist requirement by about a factor of 2.5 (*i.e* 5 pixels per resolution element). These considerations determine the position of the optics.

The off-axis imaging capabilities of this arrangement have been studied, along with those of other Wolter arrangements, such as a U configuration parabola–parabola and a Z-configuration ellipse–ellipse. The modified Wolter type 1 arrangement with a hyperbola–ellipse combination performs best and is capable of high-resolution imaging over an object field up to almost 1 mm off-axis. As the magnification increases, the object field over which high-fidelity imaging can be achieved shrinks. The choice of $M \simeq 5$ nicely matches the illumination field of the beamline onto the detector.

Fig. 4 shows the off-axis performance of the Wolter mirrors as configured in the spectrometer. It shows the FWHM of the image of a point-object at varying distance off-axis and with varying angular acceptance of the Wolter mirrors in their imaging plane. The size of the object field shrinks as the angular collection increases. This is a result of the curvature of the erect focal plane, giving a primary aberration that is simply due to the defocus displacement of the focusing circle relative to the flat image plane. Collecting 5 mrad is consistent both with the illumination field over the required range of $h\nu_{\rm in}$ and with the maximum length of the mirrors, given their position and angle.

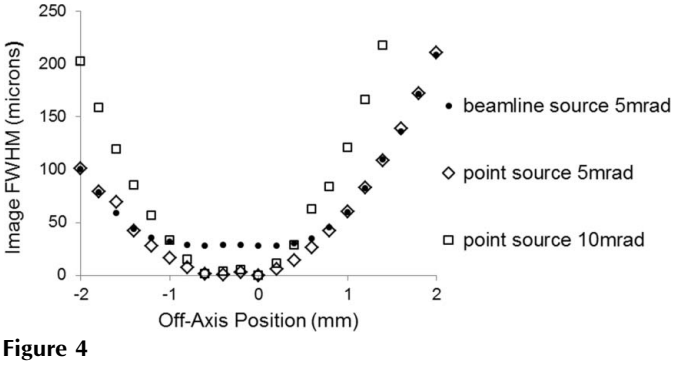

Figure 4
Vertical image width as a function of vertical off-axis position for the spectrometer, with parameters given in Fig. 3 and Table 1. The plot is for a point source on the sample and for the 5.6 μm FWHM vertical resolution element of the beamline monochromator, the beamline source. With a magnification M = 5.14, the geometric image of the beamline source has 29 μm FWHM. For an illumination bandwidth of 5 eV at 4.5 eV mm^{-1} dispersion on the sample, the Wolter mirrors must image over a 1.1 mm (FW) field and this can be accomplished with 5 mrad (FW) collection angle. Larger collection angles reduce the available field.

To extend the size of the object field, the Wolter mirrors can be operated slightly out of focus in order to balance the geometric contribution to the image size with the aberration contribution. The defocused size of a point source would still be smaller than the size of the geometrical image of the spot on the sample. The image-width curves shown in Fig. 4 would be shifted downward slightly, enlarging the off-axis field on the sample over which high-resolution imaging can be achieved.

5. Dispersive spectrometer optics

The dispersive optics consist of an elliptical focusing mirror and a plane VLS grating. The VLS is designed to produce an erect focal plane and this is easier in the case of this large-aperture design because of the fixed focusing provided by the mirror. Otherwise it could be provided entirely by the grating, but only with an extreme prescription for the VLS parameters. If the mirror were spherical its aberrations could be corrected by the VLS (the quadratic term) over a limited collection aperture. Here we want to collect over a larger aperture and, in order to avoid requiring several terms higher than quadratic in the VLS polynomial, an elliptical mirror is used instead. We also find that the orthogonal Wolter mirrors would be sensitive to any sagittal focusing of this mirror so an elliptical cylinder will be used.

High spectral resolution is achieved by combining a small image at the detector with a high value of dispersion. This is most easily achieved if the illumination spot on the sample is small in the dispersive direction. At the same time the dispersive optics must magnify this source so that a spectral resolution element at the detector corresponds to more than two pixels to satisfy Nyquist sampling. These are conflicting requirements. In positive (inside) order the grating demagnifies naturally so the mirror would need to magnify by a large factor. This means the mirror (and grating) would be close to the source. In negative (outside) order the dispersion is reduced and the grating magnifies, reducing the resolution, but the dispersive optics can move away from the source and the resolution is recovered. This latter geometry magnifies more and produces a larger resolution element at the detector and so it has been adopted here. The downside is that the elliptical mirror must be longer to collect the same angular range.

The spectrometer layout is shown in Fig. 3. The spectrometer is optimized specifically at 700 eV and the performance has been examined over a range of photon energies from 680 eV to 740 eV. This corresponds to Fe L-edge RIXS where the incoming photon energies are tuned to resonances with widths up to about 5 eV and the emission spectra may be measured up to an energy loss of about 10 eV. Measurements on different atomic species would use a different grating, with line spacing scaled with the wavelength to preserve the spectrometer geometry.

Fig. 5 illustrates the dispersive optical scheme. The variation of grating groove density (g) is represented as a polynomial,

Table 1
Spectrometer parameters suitable for a Au-coated grating.

λ_0 (nm)	g_0 (m^{-1})	g_1 (m^{-2})	g_2 (m^{-3})	g_3 (m^{-4})	u (m)	v (m)	r_A (m)	r_B (m)	C_0	α (°)	β_0 (°)	M_0(h)	M(v)
1.771	5×10^6	2.85×10^6	1.22×10^6	0	1.2	3.686	−3.486	3.5	0.301	82.0	−87.6	10.26	5.14

$$g(x) = g_0 + g_1 x + g_2 x^2 + g_3 x^3, \tag{2}$$

where x is the coordinate along the grating surface from the pole in the direction of propagation. The grating equation is

$$\sin\alpha + \sin\beta = m\lambda g_0, \tag{3}$$

where α and β are the incident and diffracted angles relative to the grating normal, with $\alpha > 0$ and $\beta < 0$. m is the diffracted order (negative is outside order) and λ is the X-ray wavelength.

The focus condition for a plane grating is

$$\frac{\cos^2\alpha}{r_A} + \frac{\cos^2\beta}{r_B} = m\lambda g_1, \tag{4}$$

where r_A and r_B are the object and image distances of the grating. $r_A < 0$ because of the virtual source for the grating.

The overall magnification of the system is

$$M = \frac{v}{u}\frac{r_B}{r_A}\frac{1}{C} \quad \text{with} \quad C = \frac{\cos\beta}{\cos\alpha} \tag{5}$$

where u and v are the object and image distances of the elliptical mirror.

The source size limit to the resolving power is

$$R_{\text{source}} = \frac{m\lambda g_0}{2.35\sigma}\frac{r_A}{\cos\alpha}\frac{u}{v} = \frac{m\lambda g_0}{2.35\sigma}\frac{r_B}{\cos\beta}\frac{1}{M}, \tag{6}$$

where σ is the r.m.s. horizontal size of the focused spot on the sample.

The focal plane tilt (ψ) of a plane grating with respect to the optical axis is given by

$$\tan\psi = -2\tan\beta - \frac{g_1 r_B}{g_0\cos\beta}, \tag{7}$$

so that for an erect focal plane ($\psi = 0$)

$$g_1 = -\frac{2g_0\sin\beta_0}{r_B}. \tag{8}$$

This is set at the design wavelength λ_0. β_0 represents the value of β at the design wavelength.

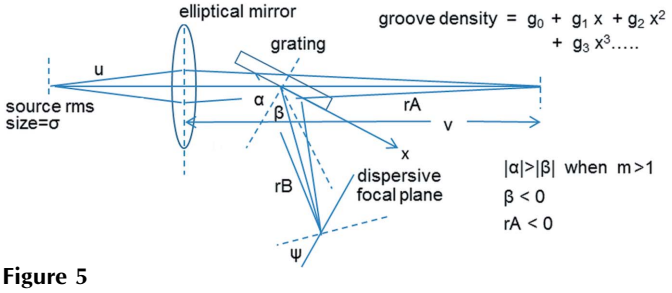

Figure 5
Optical scheme in the dispersion plane.

The focal plane is almost flat so there is negligible defocus across the energy range of a specific grating. Finally the system must be brought into focus with the optics at the required position by choosing the value of r_A,

$$r_A = \frac{\cos^2\alpha}{\left[g_1 m\lambda_0 - (\cos^2\beta_0)/r_B\right]}. \tag{9}$$

Even with an elliptical mirror, a quadratic VLS term is required to correct grating aberrations. The best value of g_2 is determined by ray-tracing and is dependent on the illuminated length of the grating.

With the geometry shown in Fig. 3, a 5000 lines mm^{-1} (Au-coated) grating in outside order ($m = -1$ with included angle $2\theta = 169.6°$; see Table 1) can give a 30000 resolving power if the (horizontal) source size is 2.3 µm FWHM. A larger included angle would need a coarser grating and the resolving power would be reduced. The magnification of the spectrometer in the dispersive plane is $M \simeq 10$, adequate for use with 5 µm detector pixels. Collecting 9 mrad FW in the dispersive direction requires an elliptical mirror 310 mm long and illuminates about 60 mm of grating length.

6. Spectrometer performance

Fig. 6 shows the basic resolution properties in the spectrometer dispersive plane around 700 eV, using the parameters in Table 1. The beamline produces a horizontal focus of 2.3 µm FWHM on the sample. This is the source for the spectrometer in its dispersion plane. The limit to the resolving power ($R_{\text{source}} \simeq 32000$) due to the 2.3 µm spot is approximately the same as that due to a 20 µm patch on the detector (R_{detector}) at $h\nu_{\text{out}} =$ 700 eV. With 5 µm pixels the spectrometer can operate at $R \simeq$ 30000 in $h\nu_{\text{out}}$, close to the source size limit, across a range of input energies ($h\nu_{\text{in}}$) corresponding (in this case) to the entire

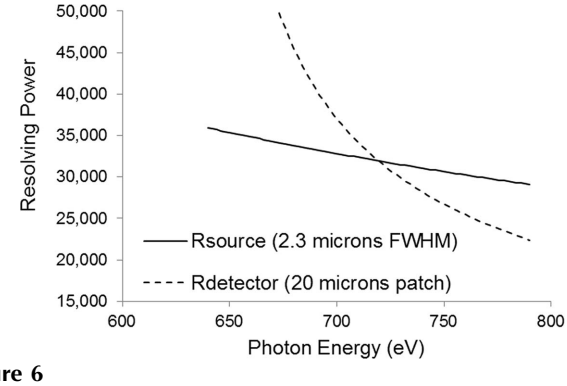

Figure 6
Limit to the resolution corresponding to the size of the spot on the sample (2.3 µm FWHM) and corresponding to a 20 µm patch of the detector.

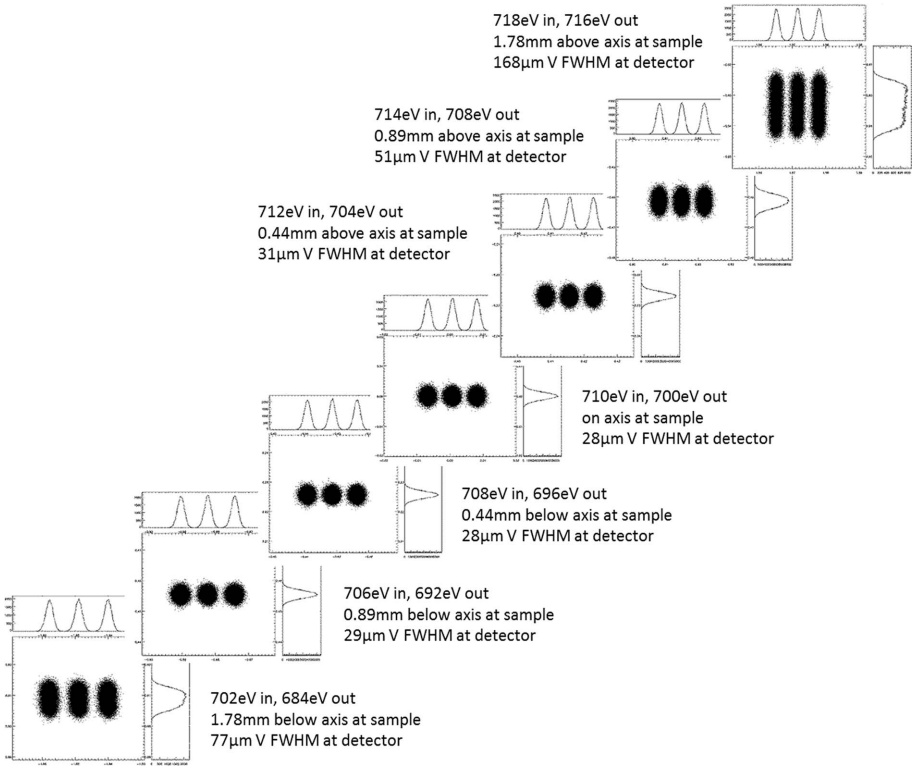

Figure 7
Ray-trace (*SHADOW*) of three emission lines separated by 1:10000 imaged at the detector. Energy loss varies from 2 eV to 18 eV over a range of incident photon energy from 702 eV to 718 eV. These seven screens are each 400 μm × 400 μm. The three lines move 3.4 mm across the detector in the dispersive direction of the spectrometer. For this computation the spectrometer is collecting ±2.5 mrad vertically and ±5.0 mrad horizontally.

L-edge of Fe. The defocus limit to the spectrometer resolving power is negligible, greater than $R \simeq 500000$ from 620 eV to 780 eV thanks to the spectrometer's flat erect dispersive focal plane.

The combined effects of the dispersive optics together with the imaging Wolter mirrors are shown in Fig. 7. This is a ray-trace study using *SHADOW* (Cerrina & Rio, 2009). Scattered photons in a group of three energies separated by 1:10000 are traced from different vertical positions on the sample, corresponding to various incident energy photons each focused by the beamline to a vertical resolution element of 5.6 μm FWHM. A range of incident energies ($h\nu_{\rm in}$) from 702 eV to 718 eV is modeled. The beamline dispersion is about 4.5 eV mm^{-1} at the sample so the sample is illuminated over a range ±1.78 mm above and below the spectrometer axis. This range of $h\nu_{\rm in}$ is much larger than would be required to cover a typical resonant peak. The axial value of the incident energy can be tuned (over the entire *L*-edge) by the beamline monochromator. Energy-loss values from 2 eV to 18 eV have been studied to make this an extreme example. High-resolution (R = 30000) mapping of the incident ($h\nu_{\rm in}$) and scattered ($h\nu_{\rm out}$) photon energy onto the detector is achieved over an incident bandwidth of 6 eV before the aberrations of the Wolter mirrors in the vertical direction begin to limit the spectral resolution of $h\nu_{\rm in}$. The design goal of a 5 eV bandwidth in $h\nu_{\rm in}$ has been met.

7. Adaptation for multilayer gratings

So far we have arranged the grating angles to work with a metal reflective coating. The efficiency of a blazed Au-coated grating with 5000 lines mm^{-1} has been computed using *GSOLVER* (http://www.gsolver.com) and we calculate 4.8% diffraction efficiency on-blaze at 700 eV using first (outside) order for a sawtooth groove profile with 2.8° blaze angle. The efficiency decreases to about 2% at 650 eV away from optimum blaze as the groove shadows grow.

An attractive feature of the spectrometer layout (Fig. 3) is that the grating is the last optic. The blazed Au-coated grating can be replaced with a blazed multilayer grating with higher efficiency without significantly modifying the mechanical design. The Au-coated grating has useful efficiency at shallow angles (included half-angle $\theta \simeq 85°$). Multilayer gratings must operate away from grazing geometry, $\theta \simeq 80°$, to have reasonable efficiency. The line density and the grating angles must be changed to reduce θ and to maximize the multilayer grating efficiency while maintaining the required source-size and pixel-size limits to the resolution. The multilayer grating would be mounted at the appropriate angle and the detector would be moved accordingly. The arm length is preserved so that the imaging in the non-dispersive plane is not affected. Fig. 8 shows the angles required for a resolving-power limit of 32000 on a 20 μm patch of the detector as the line density is increased. A multilayer grating could be implemented with

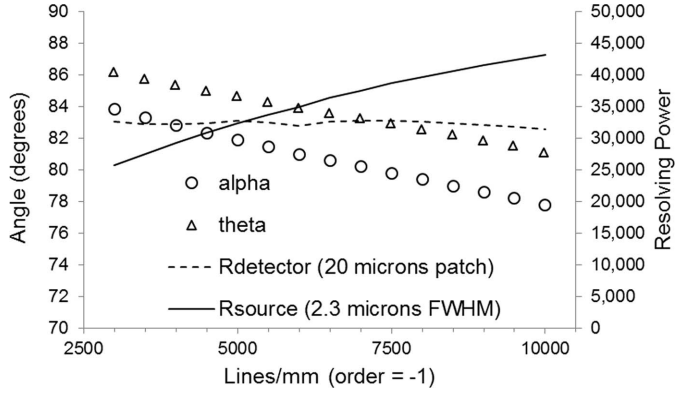

Figure 8
Gratings with various line density operated so that the resolving power of a 20 μm patch of the detector is approximately constant at $R_{\rm det} \simeq 32000$. θ is half the included angle. A gold-coated grating would have 5000 lines mm^{-1}. Multilayer gratings would operate at smaller values of α and θ and would need (effectively) higher line density.

Table 2
Spectrometer parameters suitable for a multilayer coated grating with $m = -3$.

λ_0 (nm)	g_0 (m^{-1})	g_1 (m^{-2})	g_2 (m^{-3})	g_3 (m^{-4})	u (m)	v (m)	rA (m)	rB (m)	C_0	α (°)	β_0 (°)	M_0(h)	M(v)
1.771	2.5×10^6	1.425×10^6	Not computed	0	1.2	3.680	−3.480	3.5	0.401	79.8	−85.93	7.70	5.14

Table 3
Spectrometer parameters suitable for a multilayer coated grating with $m = -4$.

λ_0 (nm)	g_0 (m^{-1})	g_1 (m^{-2})	g_2 (m^{-3})	g_3 (m^{-4})	u (m)	v (m)	rA (m)	rB (m)	C_0	α (°)	β_0 (°)	M_0(h)	M(v)
1.771	2.5×10^6	1.422×10^6	Not computed	0	1.2	3.676	−3.476	3.5	.467	77.8	−84.34	6.61	5.14

2500 lines mm^{-1} operating in the third or fourth order (Voronov *et al.*, 2010, 2012). Tables 2 and 3 show the geometric parameters of the spectrometer in each case.

Fig. 9 shows the computed efficiency of an optimized blazed grating coated with a W/B_4C multilayer in these two geometries. These computations were made both with *GSOLVER* and with *PCGrate* (http://www.pcgrate.com). The optimally blazed facets are modeled to extend over 85% of the grating period; the remainder of the grating surface is an anti-blazed facet resulting in an overall triangular groove profile. We make use of pre-processer code to build an input file for *GSOLVER* describing the multilayer grating with a rectilinear mesh. *PCGrate* is written specifically to compute efficiencies for multilayer gratings. Similar results were obtained with both codes. This grating model has a computed maximum efficiency close to 18% at 700 eV, much higher than that computed for the Au-coated grating. Fourth order is preferable to third and an actual multilayer grating might have diffraction efficiency significantly greater than 10%.

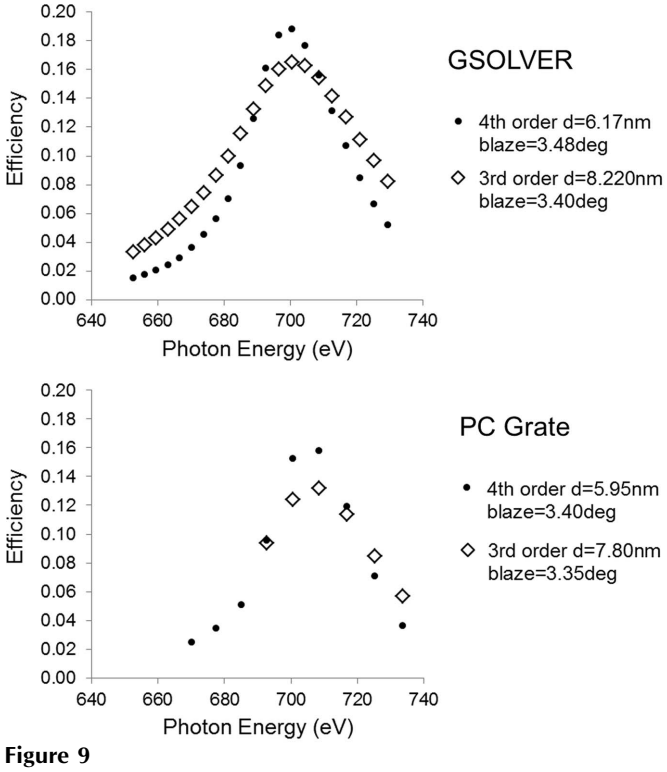

Figure 9
Computed diffraction efficiency of a blazed W/B_4C multilayer grating for this spectrometer with 2500 lines mm^{-1} operating in the third or fourth order. d is the multilayer period normal to the blazed facet and the ratio of the thickness of the heavy layer to the multilayer d-spacing is 0.3. The computations are for a triangular groove profile that is 85% blazed and 15% anti-blazed. The required blaze angle is approximately the same in each case.

8. Summary and conclusions

We have described the basic design of an imaging spectrometer that can measure a complete RIXS map in parallel.

The sample is illuminated by an undulator beam and the undulator spectral peak is dispersed vertically over the sample surface by a high-resolution monochromator with an erect focal plane. This spectrally resolved illumination covers the spectral width of a typical absorption resonance, a few eV. At the same time the beamline forms a highly demagnified image of the synchrotron source on the sample. The sample illumination is a vertical strip only a few micrometers wide.

The spectrometer views the sample from the side. It magnifies and images the illuminated sample vertically, mapping the energy of the incoming photons onto a small-pixel CMOS detector. At the same time the spectrometer disperses the emitted light horizontally and resolves the energy of the outgoing photons. Imaging in the spectrometer is by means of a modified Wolter scheme that can form an image of the erect sample on an erect detector plane over a field of the order ± 1 mm. This corresponds to a typical absorption resonance width. The dispersive spectrometer optics consists of an elliptical mirror and a plane VLS grating with high line density. These optics magnify and image onto the same erect focal plane in the orthogonal (horizontal) direction.

The overall optimization of the spectrometer satisfies many requirements simultaneously. The angular acceptance in the non-dispersive vertical direction is the most that the Wolter mirrors can collect, given their position and angle. They are positioned to provide the required magnification in the available spectrometer length. The vertical angular acceptance is the maximum possible for the size of the object field over which high-resolution imaging is required. In the dispersive direction the quadratic variation of the grating line space can correct the grating aberrations over the horizontal angular acceptance, which is the maximum allowed by the available space for the dispersive optics. The overall magnification gives a 24 μm (H) × 29 μm (V) resolution patch on the detector in

both directions, which is consistent with 5 μm pixels and about 2.5× Nyquist oversampling.

The spectrometer geometry lends itself to an upgrade to use optimized multilayer gratings. These multilayer gratings would be about three times more efficient than metal-coated gratings.

All of the technologies required for a multiplexed RIXS spectrometer have been separately demonstrated, from our own work on high-resolution grating fabrication to the manufacture of hyperbolic and elliptical formed mirrors. A key enabling technology of small pixel detectors is a critical component of the work, and initial results are showing this to be a viable approach. With all of these elements together, this design should open new avenues in the application of *q*-resolved RIXS to the study of complex correlated-electron materials.

The Advanced Light Source is supported by the Director, Office of Science, Office of Basic Energy Sciences, of the US Department of Energy under contract No. DE-AC02-05CH11231.

References

Abbe, E. (1879). *Sitz. Jena. Ges. Med. Naturwiss.* **13**, 129–142.
Amemiya, K., Kitajima, Y., Ohta, T. & Ito, K. (1996). *J. Synchrotron Rad.* **3**, 282–288.
Ament, L. J. P., van Veenendaal, M., Devereaux, T. P., Hill, J. P. & van den Brink, J. (2011). *Rev. Mod. Phys.* **83**, 705–767.
Battaglia, M., Contarato, D., Denes, P., Doering, D., Duden, T., Krieger, B., Giubilato, P., Gnani, D. & Radmilovic, V. (2010). *Nucl. Instrum. Methods Phys. Res. A*, **622**, 669–677.
Cerrina, F. & Sanchez del Rio, M. (2009). *Handbook of Optics*, Vol. V, 3rd ed., edited by M. Bass, ch. 35, *Ray Tracing of X-ray Optical Systems.* New York: McGraw Hill.
Chen, C. C., Moritz, B., Vernay, F., Hancock, J. N., Johnston, S., Jia, C. J., Chabot-Couture, G., Greven, M., Elfimov, I., Sawatzky, G. A. & Devereaux, T. P. (2010). *Phys. Rev. Lett.* **105**, 177401.
Contarato, D., Denes, D., Doering, D., Joseph, J. & Krieger, B. (2011). *Nucl. Instrum. Methods Phys. Res. A*, **635**, 69–73.
Damascelli, A., Hussain, Z. & Shen, Z. X. (2003). *Rev. Mod. Phys.* **75**, 473–541.
Fung, H. S., Chen, C. T., Huang, L. J., Chang, C. H., Chung, S. C., Wang, D. J., Tseng, T. C. & Tsang, K. L. (2004). *AIP Conf. Proc.* **705**, 655–658.
Hettrick, M. C., Underwood, J. H., Batson, P. J. & Eckart, M. J. (1988). *Appl. Opt.* **27**, 200–202.
Kodama, R., Ikeda, N., Kato, Y., Katori, Y., Iwai, T. & Takeshi, K. (1996). *Opt. Lett.* **17**, 1321–1323.
Kotani, A. & Shin, S. (2001). *Rev. Mod. Phys.* **73**, 203–246.
Matsuyama, S., Wakoika, T., Kidani, N., Kimura, T., Mimura, H., Sano, Y., Nishino, Y., Yabashi, M., Tamasaku, K., Ishikawa, T. & Yamauchi, K. (2010). *Opt. Lett.* **21**, 3583–3585.
Saha, T. T. (1987). *Appl. Opt.* **26**, 658–663.
Strocov, V. N. (2010). *J. Synchrotron Rad.* **17**, 103–106.
Voronov, D. L., Ahn, M., Anderson, E. H., Cambie, R., Chang, C. H., Gullikson, E. M., Heilmann, R. K., Salmassi, F., Schattenburg, M. L., Warwick, T., Yashchuk, V. V., Zipp, L. & Padmore, H. A. (2010). *Opt. Lett.* **35**, 2615–2617.
Voronov, D. L., Anderson, E. H., Gullikson, E. M., Salmassi, F., Warwick, T., Yashchuk, V. V. & Padmore, H. A. (2012). *Opt. Lett.* **37**, 1628–1630.
Wolter, H. (1952*a*). *Ann. Phys.* **10**, 94–114.
Wolter, H. (1952*b*). *Ann. Phys.* **10**, 286–295.
Wray, L. A., Jarrige, I., Ikeuchi, K., Ishii, K., Shvyd'ko, Y., Xia, Y., Hasan, M. Z., Mathy, C., Eisaki, H., Wen, J., Xu, Z., Gu, G. D., Hussain, Z. & Chuang, Y.-D. (2012). *ArXiv*: 1203.2397.